Landslides
DOI 10.1007/s10346-017-0901-0
Received: 9 March 2017
Accepted: 2 October 2017

Gioachino Roberti · Brent Ward · Benjamin van Wyk de Vries · Pierre Friele · Luigi Perotti · John J. Clague · Marco Giardino

Precursory slope distress prior to the 2010 Mount Meager landslide, British Columbia

Abstract In 2010, the south flank of Mount Meager failed catastrophically, generating the largest ($53 \pm 3.8 \times 10^6$ m^3) landslide in Canadian history. We document the slow deformation of the edifice prior to failure using archival historic aerial photographs spanning the period 1948–2006. All photos were processed using Structure from Motion (SfM) photogrammetry. We used the SfM products to produce pre- and post-failure geomorphic maps that document changes in the volcanic edifice and Capricorn Glacier at its base. The photographic dataset shows that the Capricorn Glacier re-advanced from a retracted position in the 1980s then rapidly retreated in the lead-up to the 2010 failure. The dataset also documents 60 years of progressive development of faults, toe bulging, and precursory failures in 1998 and 2009. The 2010 collapse was conditioned by glacial retreat and triggered by hot summer weather that caused ice and snow to melt. Meltwater increased pore water pressures in colluvium and fractured rocks at the base of the slope, causing those materials to mobilize, which in turn triggered several secondary failures structurally controlled by lithology and faults. The landslide retrogressed from the base of the slope to near the peak of Mount Meager involving basement rock and the overlying volcanic sequence. Elsewhere on the flanks of Mount Meager, large fractures have developed in recently deglaciated areas, conditioning these slopes for future collapse. Potential failures in these areas have larger volumes than the 2010 landslide. Anticipated atmospheric warming over the next several decades will cause further loss of snow and glacier ice, likely producing additional slope instability. Satellite- and ground-based monitoring of these slopes can provide advanced warning of future landslides to help reduce risk in populated regions downstream.

Keywords Landslide · Mount Meager volcano · Glacial retreat · Slope deformation · Historical airphotos

Introduction

Large landslides and debris flows are common on the slopes of active and inactive volcanoes, and especially those that presently support glaciers or that have been incised by glaciers and streams in the past. Although many researchers have examined the relationship between deglaciation and volcanic eruptions (Rampino et al. 1979; Jellinek et al. 2004; Huybers and Langmuir 2009; Watt et al. 2013) and between eruptions and large-scale collapses of volcanic edifices (Voight et al. 1981, 2002; Siebert 1984; Glicken 1996), investigations of deglaciation as a mass wasting trigger in volcanic environments are few; notable exceptions include Holm et al. (2004), Capra (2006), and Capra et al. (2013), and only recently have researchers begun to document non-eruptive landslides from presently ice-clad volcanoes (e.g., Huggel et al. 2007, 2008).

Glaciers can destabilize volcanic edifices in many ways. They abrade and fracture already weak, highly fractured flows and pyroclastic deposits and remove support from the base of oversteepened slopes, changing the stress regime and further decreasing their stability (Huggel 2009; McColl et al. 2010; Grämiger et al. 2017). Water from melting ice easily enters these fractured rocks, increasing pore water pressure, which in turn causes instability (Terlien 1998). In active volcanoes, heated fluids also hydrothermally alter and further weaken host rocks (Reid et al. 2001; Finn et al. 2001; Pola et al. 2012, 2014; Wyering et al. 2014). Saturated, weakened, and altered rocks may deform by creep processes (Cecchi et al. 2004; Pola et al. 2014; Heap et al. 2015; Heap and Wadsworth 2016), inducing gravitational distress that can culminate in collapse (van Wyk de Vries and Francis 1997; Cecchi et al. 2004). Large amounts of water may be stored in the porous and permeable rocks of the volcanic edifice (Delcamp et al. 2016; Detienne 2016) and, in the event of a deep-seated collapse of a volcanic flank, can transform a simple rockslide into a mobile debris avalanche or debris flow (Roverato et al. 2011; Capra et al. 2013; Delcamp et al. 2016; Roberti et al. 2017).

The Mount Meager volcano (Fig. 1) is a good example of a volcanic edifice that is susceptible to failure conditioned by the aforementioned processes. It has been deeply dissected by glaciers and subject to glacier retreat, leaving steep slopes in volcanic and basement rocks that have been subject to hydrothermal alteration. A rich archive of historical aerial photographs (1948, 1964–1965, 1973, 1981, 1990, and 2006) is available to document more than one-half century of topographic changes caused by gravitational deformation.

On 6 August 2010, the south flank of Mount Meager failed, generating a large debris avalanche that traveled down the valleys of Capricorn and Meager creeks and into the Lillooet River valley nearly 13 km from the source (Fig. 1) (Guthrie et al. 2012; Allstadt 2013; Moretti et al. 2015). Roberti et al. (2017) describe the deposit of this landslide and interpret its kinematics and dynamics. Here, we complement previous studies with an assessment of the source area of the landslide in the lead-up to the catastrophic failure of 2010. Using high-resolution digital elevation models (DEMs) generated from aerial photographs, we track both deformation of the slope and the activity of Capricorn Glacier at its toe over a 62-year period. Mapping of lithologic units and structures exposed in the rock slope allowed us to document slow progressive deformation. We refine the previous volume estimate of the failed rock mass (Guthrie et al. 2012) and estimate its water content. Merging our observations of precursory slope distress with the seismic record of the collapse (Allstadt 2013), we infer a retrogressive failure sequence. Finally, we discuss the effects of hydrothermal alteration, continuing deglaciation, and groundwater storage on the stability of the larger Mount Meager volcanic complex, as well as the factors that condition and could trigger failures in the future.

Context of the Mount Meager failure

The Mount Meager volcano is a partially glacier-covered volcanic complex located in the southern Coast Mountains of southwest British Columbia, 60 km northwest of the town of Pemberton (Fig.

Published online: 18 October 2017

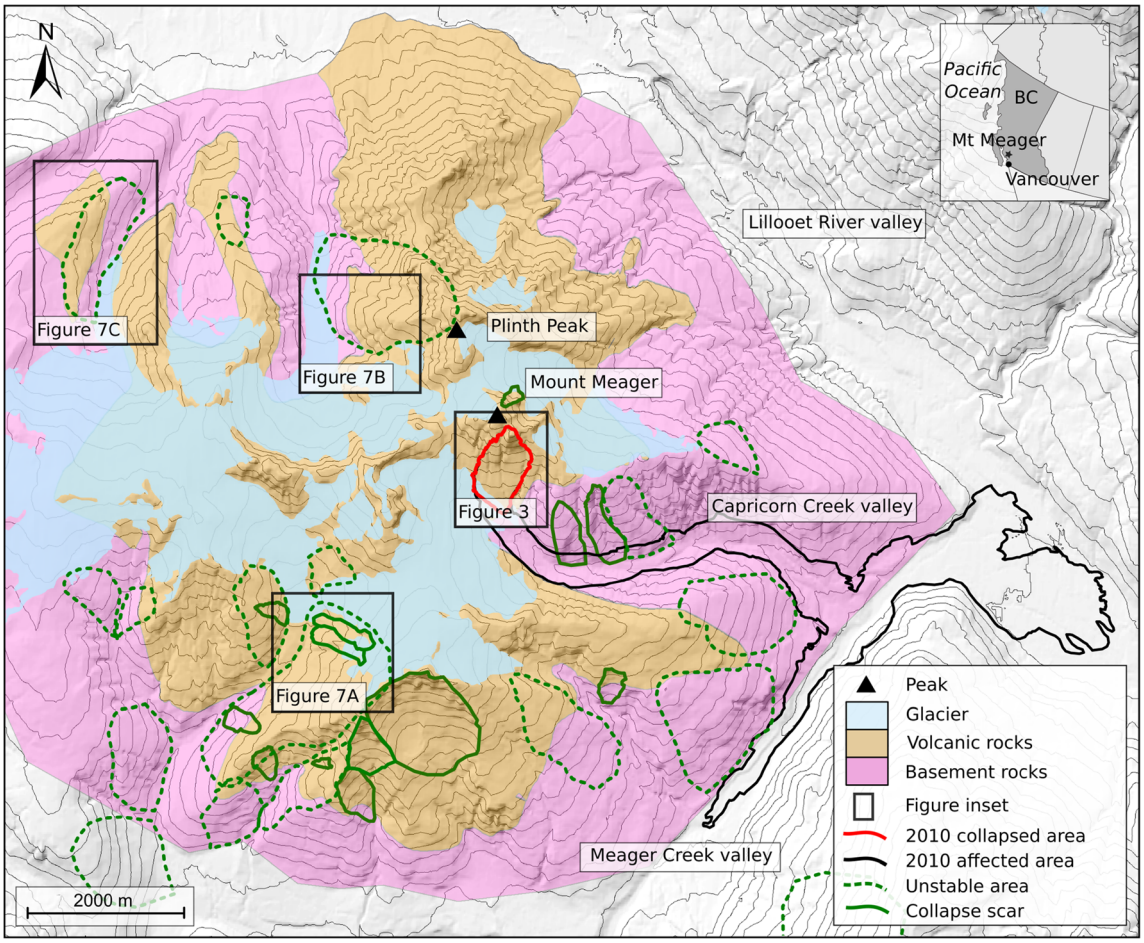

Fig. 1 Location map and geology of Mount Meager volcanic complex (geology after Read 1978). Also shown is the headscarp and deposit of the 2010 landslide, as well as other gravitational instabilities in the area. Inset map shows the location of Mount Meager in British Columbia (BC) on the west coast of Canada

1). It is a coalescent group of volcanic centers of Pliocene to Holocene age that have been built on top of Mesozoic granitic and metamorphic basement rocks (Read 1978, 1990). The last eruption, from near Plinth Peak, happened about 2400 years ago and produced a small flow, ignimbrite, and a plume of ash that reached as far east as the Alberta Rocky Mountains (Clague et al. 1995; Hickson et al. 1999). The volcano comprises a suite of eruptive products, including pyroclastic rocks, basalt flows, and rhyodacite domes (Read 1978, 1990). Parts of the volcanic pile have been hydrothermally altered, and active fumaroles and hot springs are present on the flanks of the massif. The area was repeatedly glaciated by ice caps and the Cordilleran Ice Sheet during the Pleistocene (Clague and Ward 2011) and presently supports numerous small glaciers. The volcanic and basement rocks have been deeply dissected by glacial and fluvial erosion and by mass movements, leaving steep slopes and a current local relief of up to 2200 m.

The Mount Meager volcano has been the site of numerous prehistoric and historic landslides (Friele et al. 2008). The most recent large landslide, which happened on 6 August 2010, involved over 50 × 10^6 m^3 of highly fractured and altered volcanic and basement rocks on the south flank of Mount Meager. The path height of 2185 m and the maximum path length of 12.7 km yield a *Fahrböschung* (travel angle) of 9.8°. The landslide generated an equivalent magnitude 2.6 earthquake, and long-period seismic waves were recorded at stations as far away as southern California and northern Alaska. Examination of the seismograph records suggested that the peak velocity of the landslide was 90 m/s and the collapse occurred retrogressively. Based on the seismic data, Allstadt (2013) concluded that the primary failure occurred in two stages separated by about 20 s, followed 40 s later by a smaller collapse, and finally, about 2 min later, by a fourth and final failure.

The failed area was partly covered by glaciers at the peak of the Little Ice Age (ca. AD 1570–1900; Grove 1988; Matthews and Briffa 2005). Much of this ice was lost due to climate warming in the twentieth and early twenty-first centuries (Bovis and Jakob 2000; Holm et al. 2004), and today the flanks of Mount Meager are largely ice-free. The 2010 and other large landslides on the Mount Meager volcano stem, in part, from glacier erosion and retreat and attendant stress changes of its unstable slopes (McColl et al. 2010; Grämiger et al. 2017) and, in part, from the low strength of the fractured and hydrothermally altered volcanic rocks that underlie the volcano (Evans and Clague 1994; Holm et al. 2004). Recent thaw of alpine permafrost also may have contributed to instability through the loss of ice cohesion and the liberation of water in

near-surface rocks and sediments (Geertsema et al. 2006; Allen et al. 2009).

Elevated pore water pressures may have triggered the 2010 landslide because it occurred at the end of a lengthy, late summer heatwave that exacerbated glacier melt and permafrost thaw. The link between rapid snow and ice melt during hot weather has been noted in the case of other large landslides at Mount Meager (Mokievsky-Zubok 1977; Bovis and Jakob 2000; Holm et al. 2004) and in other alpine areas (Chleborad 1997; Gruber et al. 2004; Gruber and Haeberli 2007; Harris et al. 2009; Keiler et al. 2010). Based on this relation, road-building and forestry operations in the Meager Creek watershed had been suspended before the landslide occurred.

Methods

Structure from Motion

Topographic modeling is becoming more accessible and more widely used due to recent advances in digital photogrammetry (James and Robson 2012; Remondino et al. 2014; Micheletti et al. 2015; Smith et al. 2015; Kolzenburg et al. 2016). For this study, we processed digitized historic aerial photographs and digital oblique photos with the Structure from Motion (SfM) and multi-view-stereo (MVS) algorithms (Snavely et al. 2008; James and Robson 2012; Westoby et al. 2012; Fonstad et al. 2013; Micheletti et al. 2015) to produce 3D topographic models from which orthophotos and DEMs were subsequently created.

A large set of historical British Columbia government vertical aerial photographs is available for the Mount Meager area with photo sets from 1947, 1948, 1962, 1964–1965, 1973, 1981, 1990, and 2006. The photographs are available only as paper copies produced from the original negatives, and many of them are in poor condition (i.e., deformed by humidity, scratched, or ink-annotated). In addition, metadata on the camera and flight mission are not, in all cases, available. It would be difficult, if not impossible, to process these photos using classic stereo-photogrammetric techniques. Fortunately, we were able to construct high-quality orthophotos and digital surface models (DSMs) using Structure from Motion software.

We processed and analyzed photographs from 1948, 1964–1965, 1973, 1981, 1990, and 2006 to chronicle the evolution of the massif. The 1947 and 1962 photos were not processed because the area of interest was covered by clouds in 1947 and by snow in 1962. We took oblique digital photographs with a single-lens reflex (SLR) camera during a low-level helicopter flight 23 days after the failure. Comparison of the DEMs produced from 2006 and 2010 photos allowed us to refine the estimate of the volume of the failed rock mass and to compare the source area before and after the landslide. We made field observations of the 2010 landslide source area in 2016 to ground-truth the geology as mapped by Read (1978, 1990) and to map structures in the scar left by the landslide.

Quality assessment

The SfM-MVS workflow generates 3D models in arbitrary object coordinates. The precision of the model depends on the image quality and the 3D reconstruction algorithm. The cartographic accuracy of the final orthophoto and DEM depends on the accuracy of the geographic coordinate source used in the georeferencing process. We scanned all photos at 800 DPI, following Linder's (2009) guidelines. The pixel size of digitized airphotos depends on the scanning resolution and on the approximate scale factor of the photograph (Supplemental File 1). The resulting 3D models have reconstruction errors of 0.9–1.8 pixels and precision of 0.4–1.5 m (Table 1).

When georeferencing scanned images, it is preferable to use coordinates from a source with high accuracy (ASPRS 2014); a common approach is to perform a differential GPS field survey. For this study, it was not feasible to perform such a survey due to the inaccessibility of much of the source area and danger of rock falls. Instead, we used georeferenced points on British Columbia Government standard base maps. Planimetric coordinates were derived from SPOT 10-m resolution imagery, and elevations were extracted from the Canada TRIM (Terrain Resource Inventory Map) DEM (18.3-m average accuracy) (NRCan 2013). We calculated the overall positioning accuracy based on FGDC (1998) and ASPRS (2014) recommendations. The resulting horizontal accuracy with 95% confidence (HA 95) is 15–42 m and the vertical accuracy with 95% confidence (VA 95) is 17–63 m (Table 1).

Glacier area errors

We mapped the snout of Capricorn Glacier, which lies at the base of the failed slope, on each georeferenced orthophoto. Uncertainties in the mapped extent of the glacier are related to inherent errors in the base map, errors introduced by manually tracing the margins of the glacier, and to problems in discriminating ice, snow, and snow-covered ice. To account for these errors, we buffered the perimeter of the glacier based on the cartographic precision of the orthophoto. The uncertainty includes both base map errors and errors related to ice-margin tracing. The final precision for the glacier area estimates was calculated as the root of the squared sum of buffer areas (Diolaiuti et al. 2012; D'Agata et al. 2013). Changes in the area of the glacier over time are shown in Fig. 2.

Volumetric errors

We compared topography derived from British Columbia airphotos acquired in 2006 with that derived from the post-landslide 2010 oblique helicopter photos at a pixel-by-pixel level to estimate the volume of the failed rock mass. To minimize errors in this exercise, we co-registered the two surfaces by matching recognizable points in the 3D models. To assess this error, we compared the two surfaces in areas where no significant change would be expected and assumed the same error would be present where the mass failed (Gardelle et al. 2013). The standard deviation (σ) in the elevation difference is ± 6 m. The resulting uncertainty in the volume estimate is expressed as volumetric variation (σ_{vs}) and is defined by the mean of the formula $\sigma_{vs} = \sigma A$, where the area (A) of the failed rock mass is 6.4×10^5 m^2. The volumetric error calculated in this manner is ± 3.8×10^6 m^3. We estimated the volume of the 2010 landslide by differencing the 2006 and 2010 DEMs. A small failure from the source area in 2009 had a volume of about 2–3 $\times 10^5$ m^3 (Friele 2009); we did not subtract this volume from our estimate as it is only a fraction of the calculated error.

Guthrie et al. (2012) obtained an estimate of the volume of the 2010 Mount Meager landslide of 48.5×10^6 m^3 by differencing a pre-event 25-m-resolution TRIM DEM developed from 1987 stereo-photos and a post-event 5-m-resolution DEM derived from GeoEye stereo imagery obtained in August and September 2010.

Table 1 Precision and accuracy of the different photo datasets

Year	Pixel size (m/pix)	Error pixel (m)	Precision (m)	HA 95[a] (m)	VA 95[b] (m)
2006	0.42	1.15	0.48	32.01	17.17
1990	0.51	0.91	0.46	29.68	23.46
1981	0.65	0.36	0.23	35.5	16.09
1973	0.43	1.8	0.77	15.15	22.96
1964	1.13	1.37	1.55	36.52	63.92
1948	0.93	1.14	1.06	12.82	23.00

[a] HA 95 Horizontal accuracy at 95% confidence

[b] VA 95 Vertical accuracy at 95% confidence

They did not clearly state the potential error in the estimate, but it is likely ± 15%, or ± 7.27 × 10^6 m^3 (Moretti et al. 2015), given that the pre-event DEM had a resolution of 25 m (Guthrie et al. 2012). Other uncertainties in the volume estimate stem from the fact that landslides in 1998 and 2009 affected the source scarp between the 1987 photo date and the 2010 landslide.

Results

Glacier change

Glaciers in the southern Coast Mountains began to retreat significantly from their Little Ice Age maximum positions shortly after the start of the twentieth century (Koch et al. 2009). There was a short-lived re-advance of most glaciers in British Columbia around the middle of the century. Between 1948 and 1973, Capricorn Glacier area increased at an average rate of 3 × 10^3 m^2/year. The average rate increased to 28 × 10^3 m^2/year between 1973 and 1981. Soon thereafter, the glacier again began to retreat. It retreated at an average rate of area loss of 31 × 10^3 m^2/year between 1981 and 1990, and of 12 × 10^3 m^2/year between 1990 and 2006. By 2006, the glacier had retreated past the base of the slope that would fail in 2010, and only a patch of debris-covered ice remained.

Pre-event flank conditions, 1948–2006

Prior to the 2010 landslide, the south face of Mount Meager extended from 1700 m a.s.l. at its base in upper Capricorn Creek to 2550 m a.s.l. at the summit peak. We subdivide this face into two areas (Fig. 3). The upper portion, leading to the peak, was nearly vertical with rock cliffs and pinnacles; the lower portion, formed in fractured rock and covered in part by colluvium, had a convex glacially undercut profile (red line in Fig. 4). These two parts of the face were separated by normal faults (Fig. 3). Faults further subdivided the lower portion of the face into west (W) and east (E) sectors. The W sector was bordered by a fault striking W-E and dipping south; it intersected the slope at about 2050 m a.s.l. The E sector was bordered by a fault striking NW-SE and dipping southwest; it intersected the slope at about 2200 m a.s.l. The base of the unstable area was located at about 1700 m a.s.l. at the Little Ice Age trimline of Capricorn Glacier. Between 1948 and 2006, displacements increased along normal faults and the density of faults increased (Fig. 3) as the toe progressively bulged (Fig. 4). This progressive deformation led to the landslides in 1998 and 2009 (Fig. 3f).

The sequence of changes in the slope that would fail catastrophically in 2010 is as follows:

- 1948. Faults that delineate the W and E sectors are present. The W sector is well defined, but it is not internally dissected by minor faults. The bounding fault in the E sector is present but does not appear connected to its counterpart in the W sector. Snow covers the toe of the slope, obscuring detail in that area (Fig. 3a).
- 1964–1965. Minor faults have developed in the W sector. The west side of the toe shows widely spaced faults (Fig. 3b), and the east side is dissected by three deep gullies.
- 1973. The west sector of the toe has bulged, and a large volume of colluvium and fractured and altered rocks (~ 1.5 × 10^6 m^3) on the east side of the toe has been removed by erosion (Fig. 3c).
- 1981. The area is mostly covered by snow, obscuring morphological and structural detail (Fig. 3d). Minor faults probably continued to propagate, and rock continued to degrade.
- 1990. Fractures in the W sector are wider, and the toe has further deformed and eroded (Fig. 3e).

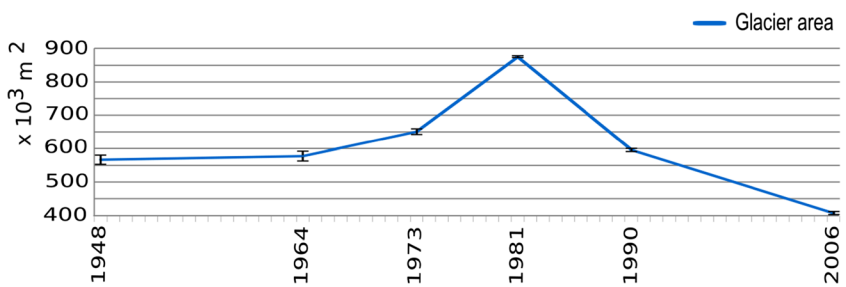

Fig. 2 Change in extent of Capricorn Glacier over the period of the photographic record. Note the re-advance of the glacier that culminated around 1981, followed by rapid retreat to the present. Error bars are shown in black

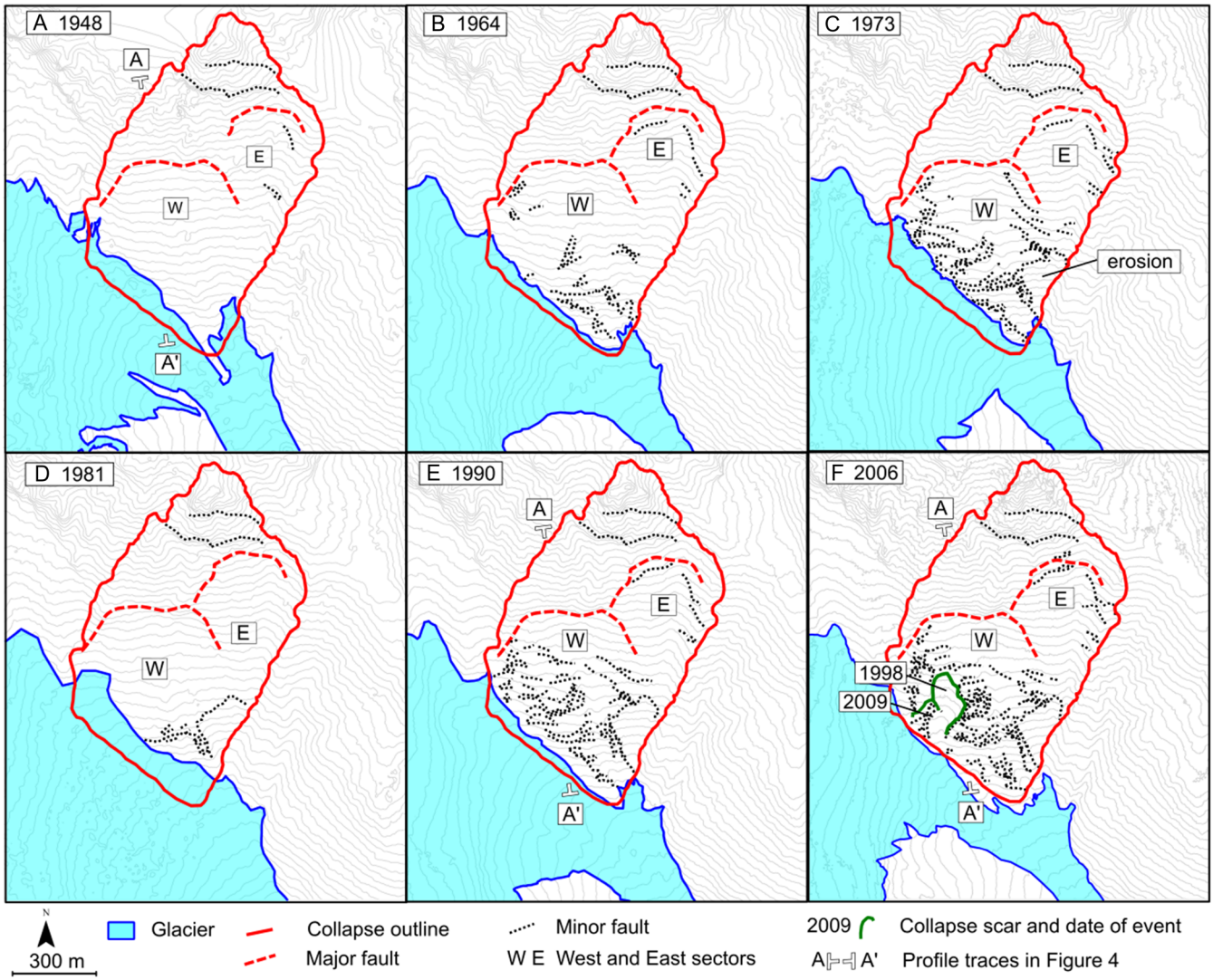

Fig. 3 Maps of the headscarp area of the 2010 landslide from 1948 to 2006. Locations of the margin of Capricorn Glacier through time, the outline of the 2010 headscarp, and faults are shown. **a** 1948: Major faults are already present. **b** 1964–1965: Diffuse deformation at the toe of the slope. **c** 1973: A large portion of the slope toe (~ 1.5×10^6 m^3) has been removed by erosion, and major and minor faults have expanded. **d** 1981: Snow covers most of the area. Capricorn Glacier is at its maximum twentieth century extent. **e** 1990: Diffuse deformation and some bulging at the toe of the slope. **f** 2006: Diffuse deformation, bulging, the scar of the 1998 landslide, and the source area of the 2009 event

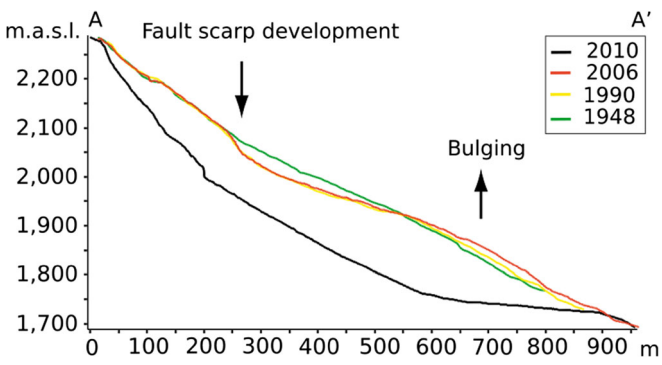

Fig. 4 Topographic cross-sections of the flank of Mount Meager in 1948, 1990, 2006, and 2010. Note major faulting, sagging, and bulging of the toe of the slope in the lead-up to the 2010 landslide. Arrows show relative directions of motion

- 2006. Four years before the catastrophic collapse, the fault delineating the W sector has accumulated 10–40 m of displacement, decreasing eastward. The bounding fault of the E sector has up to 15 m of displacement. The toe area includes the headscarp of the 1998 landslide (Bovis and Jakob 2000) and is marked by horst and graben structures (Figs. 3f and 5a).

2010 collapse

The 2010 failure involved the entire edifice sequence from the basement to the ridge crest. The estimated volume of the collapse is $53 \pm 3.8 \times 10^6$ m^3. We estimated sector volumes by parsing the slope using mapped faults: 24.6×10^6 m^3 for the W sector, 13.8×10^6 m^3 for the E sector, 9.0×10^6 m^3 for the portion above the W sector, and 5.6×10^6 m^3 for the rock peak.

The detachment surface is a step-shaped amphitheater with a steep upper section (60–90°) that is 200 m high on the east and a less steep (5–40°) lower portion. The lower basal sliding surface is located within igneous basement rocks judging from the position of adjacent basement outcrops outside the scar (Fig. 5b). Rocks involved in the failure are, from top to bottom, an intrusive rhyodacite plug, block and ash layers, volcanic breccia, and quartz diorite basement (Fig. 5b). The volcanic rocks are part of the Capricorn (0.09 Ma) and Plinth (0.1 ± 0.02 Ma) assemblages of Read (1978, 1990). The rhyodacitic plug forms the peak of the mountain; the other units are present on the lower portion of the scar and are now partly covered by talus (Fig. 5b).

1. Intrusive rhyodacite plug (unit P9i of Read 1978). This unit is pervasively fractured, with meter-scale steep columns and horizontal fractures. Parts of the unit display ochre-colored hydrothermal alteration.
2. Block and ash layers. Read (1978) mapped this unit as rhyodacitic lava flows (unit P9f). However, no lava flows are evident in the scar and the surrounding area. Rather, block and ash layers form a carapace surrounding the intrusive plug. The layers have thicknesses of several meters and dip 30–40°.
3. Volcanic breccias (unit P8x of Read 1978). These basal breccias are fractured and hydrothermally altered.
4. Quartz diorite (unit Mqd of Read 1978) unconformably underlies the volcanic sequence. The contact was covered by debris soon after the 2010 landslide, but it can be seen at the margins of the scar (Fig. 5b). Lithological analysis of the landslide deposit by Roberti et al. (2017) showed that it contains ~ 20–30% basement rock, some hydrothermally altered.

The lower part of the source slope has been intensively hydrothermally altered. Moving upward in the sequence, the block and ash layers are relatively fresh and the rhyodacite plug is only locally altered.

Meteorological trigger

Landslides at Mount Meager in 1975 and 1998 occurred during hot weather in late July and early August, respectively (Fig. 6;

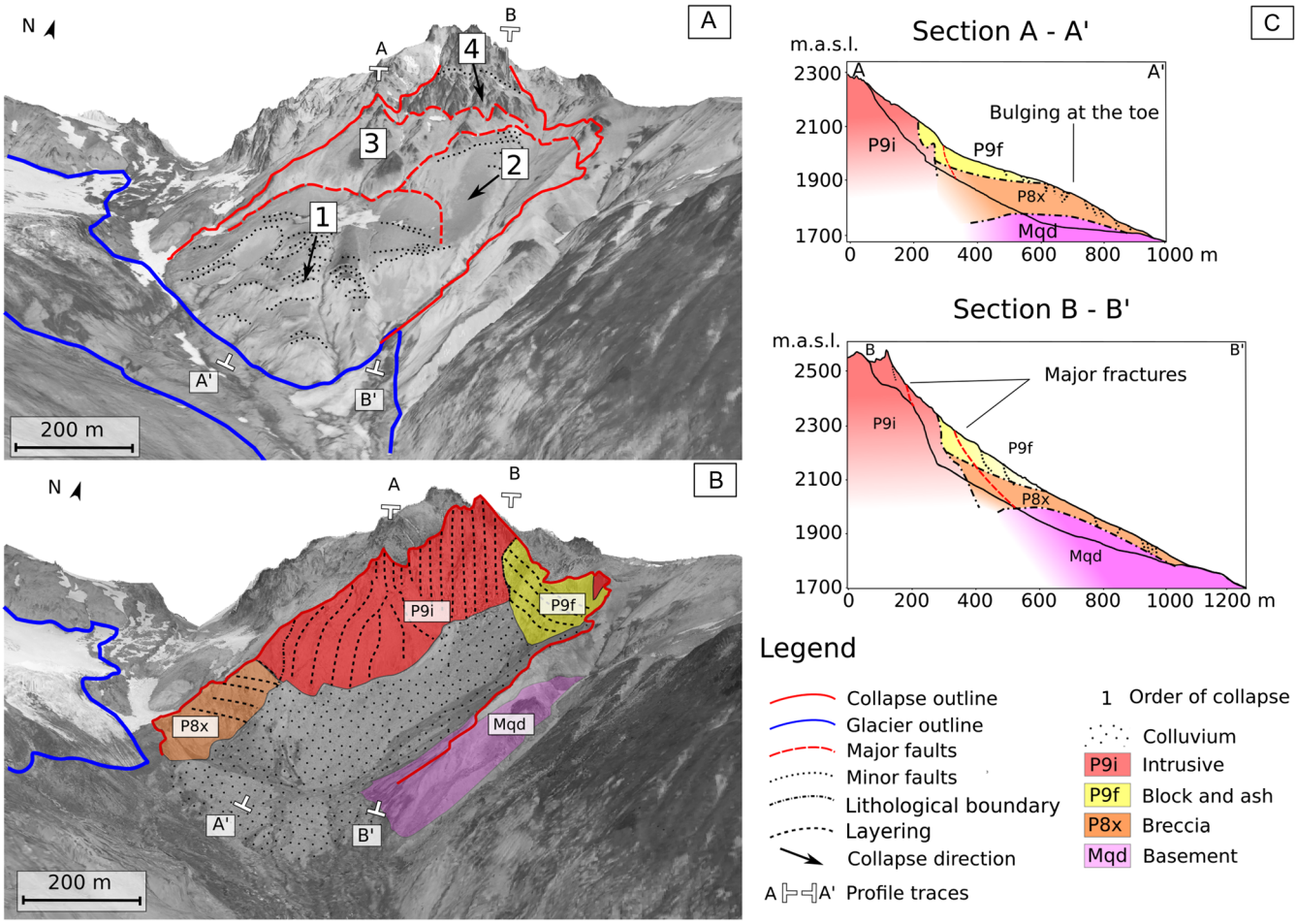

Fig. 5 **a** Flank of Mount Meager 4 years before the collapse in 2010 (modified from Delcamp et al. 2016), showing the headscarp of the landslide, failure domains, directions of collapse, faults, and the terminus of Capricorn Glacier. (1) First failure: direction of movement 191°; volume 24.6×10^6 cm^3. (2) Second failure: direction of movement 217°; volume 13.8×10^6 m^3. (3) Third failure: direction of movement mainly vertical; 40 s after the two main failures; volume 9.0×10^6 m^3. (4) Fourth failure: direction of movement mainly vertical toward the SE; 2 min after the third failure; volume 5.6×10^6 m^3. Movement directions and timing from Allstadt (2013). **b** Headscarp of 2010 landslide after the collapse (modified from Delcamp et al. 2016), showing bedrock units described in the paper. **c** Pre-and post-failure cross-sections of the source area. m.a.s.l. meters above sea level

Mokievsky-Zubok 1977; Bovis and Jakob 2000). Given this history, summer temperatures and precipitation are now monitored to control operational shutdowns at work sites around the volcano (Friele 2012). In September 2009, a landslide destroyed the road crossing at Capricorn Creek (Friele 2009). In 2010, work undertaken to repair the crossing was shut down due to a sustained heatwave in late July and early August. The 6-day running mean of daily maximum temperatures recorded by an automated station near the mouth of Capricorn Creek exceeded 28 °C from July 18 to August 5, just prior to the catastrophic failure. Maximum temperatures peaked between July 24 and 31, when the 6-day running mean exceeded 32 °C (Fig. 6).

Water in the source rocks

Immediately after the 2010 collapse, abundant water was observed issuing from the scarp and accumulating in a pond at its west edge. Seepage continued in the days following the landslide (Delcamp et al. 2016). The largest visible spring was on the west side of the headscarp at about 1800 m a.s.l., near the source of the failures in 1998 and 2009. A small glacier and permanent snow field about 500 m above and to the northwest of this spring may have fed water into the slope. Seepage was also observed on the east side of the scar at about 2100 m a.s.l., fed by the glacier sitting on the other side of the ridge crest. At the same elevation, just outside of the scar, springs in the block and ash flow deposits marked the local water table. Above this level, the upper portion of the slope is highly fractured and likely well drained.

Based on the locations of the seepage zones in the scarp, we estimate that at least 40% of the rock mass that failed (21×10^6 m^3) contained abundant water. Altered and fractured volcanic rocks can store up to 30% water by volume (Delcamp et al. 2016), leading us to estimate a maximum 6×10^6 m^3 of water was released from the rock mass upon failure.

Discussion

Glacier activity

The activity of Capricorn Glacier between 1948 and 2006 is consistent with that of other glaciers in the southern Coast Mountains (Koch et al. 2009). In spite of brief advances between the 1950s and 1970s, most small glaciers in this region have lost about half of their mass since the end of the Little Ice Age (Bovis and Jakob 2000; Holm et al. 2004; Koch et al. 2009). Capricorn Glacier loaded and then unloaded the south flank of Mount Meager. It eroded rock from the toe of the slope, while water from glacier and snow melt penetrated the volcanic rocks of the massif.

Progressive failure

Major faults that controlled the 2010 failure were already present in 1948. In the following years, displacements on these faults increased and an array of minor faults appeared, accompanied by bulging and precursory collapses at the toe of the slope (Fig. 4). The bulging toe was eroded by meltwater, further destabilizing the slope above. Bulging of the toe increased rock damage and likely fractured rock bridges along the future failure plane, reducing the overall factor of safety.

The detachment surface and the failure sequence were structurally controlled. The basal sliding surface projects to the thalweg of the glacially eroded Capricorn Creek valley. The base of this detachment includes volcanic breccia and basement rock. Rocks in the lower portion of the sequence are altered and saturated. The formation of a pond at the toe of the failed rock mass immediately after the event (Delcamp et al. 2016) indicates that rocks along the basal sliding surface had low permeability. It seems likely that at least part of this surface followed a boundary between altered, fractured basement rocks and less permeable, less fractured basement rocks.

The failure sequence consisted of four phases. The initial failure involved the fault-bounded W and E sectors of the lower part of the slope (Fig. 5a). Failure of the W and E rock masses generated the two initial pulses recorded by seismographs. Allstadt (2013) extracted the directions taken by the failing rock masses from the seismic records. The direction of the first pulse was 191°; we interpret this to record failure of the W sector, which was controlled by a W-E-striking, S-dipping fault. The direction of the second pulse, which immediately followed the first, was 217°; we interpret this to record the failure of the E sector, controlled by the NW-SE-striking fault system. Volumes calculated from the geometry of the faults indicate failures of 24.6×10^6 m^3 in the W sector

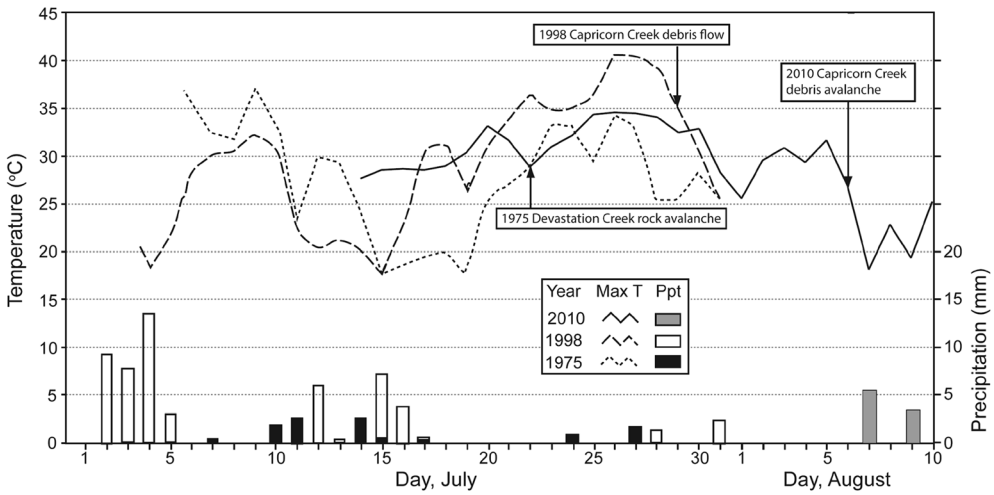

Fig. 6 Daily maximum temperature and daily total precipitation at Pemberton over the period 1 July–10 August 1975, 1998, and 2010 in relation to landslides (modified from Bovis and Jakob 2000). The 1975, 1998, and 2010 landslides happened after sustained summer heatwaves. No significant precipitation is recorded during the three periods. Max T maximum daily temperature, Ppt precipitation

and 13.8 × 10^6 m^3 in the E sector (Fig. 5). This result differs from estimates derived from numerical modeling (Moretti et al. 2015), which yielded 14 × 10^6 m^3 and 27.5 × 10^6 m^3, respectively, for the first and second stages of the landslide. We believe our estimates are valid as they are based on observed structures, rather than calibration from a numerical model.

The two primary failures left the upper part of the edifice unsupported, leading to a third failure above the W sector, which we estimate to have had a volume of 9.0 × 10^6 m^3. Two minutes later, the fourth and final phase involved collapse of the unsupported secondary peak, with a primarily vertical fall toward the SE (Allstadt 2013). A change in slope divides the secondary peak into two rock masses with individual volumes of about 2.8 × 10^6 m^3 (Fig. 5a). Separate, although nearly contemporaneous, failure of these rock masses supports Allstadt's (2013) inference that this last phase consisted of two sub-failures. Our estimate of the total volume of the fourth event (5.6 × 10^6 m^3), however, differs substantially from Allstadt's estimate (0.3 × 10^6 m^3), which is based on the magnitude of the generated force derived from seismic data.

Lithological zoning in the source area is replicated to some extent in the landslide deposit, i.e., the deposit exhibits remnant stratification (Voight et al. 1981; van Wyk de Vries et al. 2001; Valderrama et al. 2016). Highly altered rocks are found at the base of the scarp, consistent with the abundance of these rocks in the distal debris. In contrast, the peak consists of an intrusive volcanic unit, which dominates the debris at the mouth of Capricorn Creek (Roberti et al. 2017).

Causes and failure mechanism

Granitic and metamorphic rocks underlie Capricorn Creek valley and some of the adjacent lower slopes. Volcanic rocks unconformably overlie these basement rocks and are covered in many places by snow and ice. The condition of the basement is not known at all sites, but judging from exposures at the head of Capricorn Creek, these rocks are likely to be fractured and altered for some distance below the volcanic contact. The presence of weak rocks at the base of the volcano can have a strong destabilizing effect (van Wyk de Vries et al. 2001; Cecchi et al. 2004; Detienne 2016), and large volumes (> 5 × 10^6 m^3) of rock can undergo gravitational damage and displacement (Kilburn and Petley 2003).

Inflow of meltwater during the warm summer of 2010 likely elevated pore water pressures beneath the steep south slope of Mount Meager. The reduction in effective stress, coupled with the progressive removal of support at the toe by erosion and fracturing induced by slow deformation, brought the slope to catastrophic failure (two loud cracks heard by the witnesses; Guthrie et al. 2012). The weight of the overlying stratigraphic sequence pushed out the basal breccia and basement units, leading to the collapse of the slope above. The first force generated by the collapse had a mainly

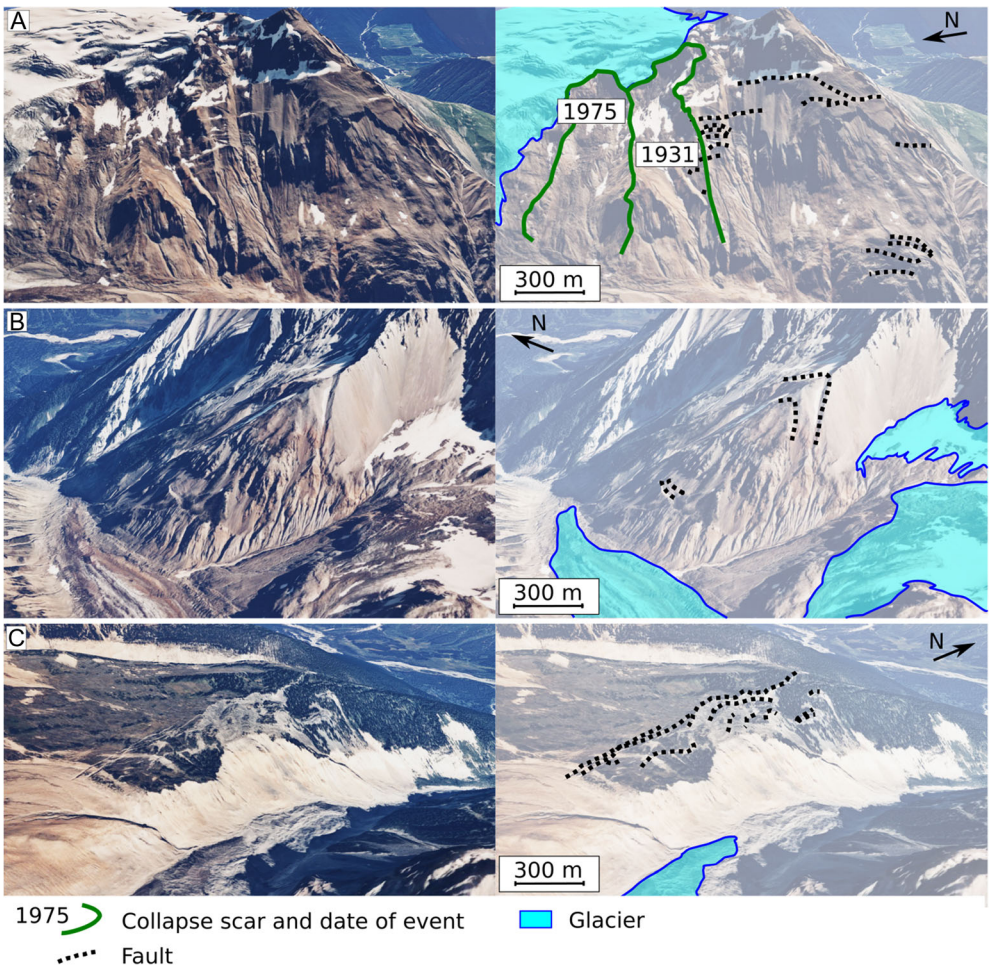

Fig. 7 Continuing instability on the Mount Meager volcano. **a** East flank of Devastation Creek valley. **b** West flank of Plinth Peak. **c** West flank of Affliction Creek valley

horizontal orientation and a slow initial acceleration of 0.39 m/s^2 (Allstadt 2013). The large amount of water expelled from the moving rock mass (up to 6×10^6 m^3) generated a debris avalanche with a water-rich front and water-poor core (Roberti et al. 2017).

The slow initial acceleration, large volume of the failure, and presence of hydrothermally generated clays and fluids fit the slow, self-cracking model proposed by Kilburn and Petley (2003). Large catastrophic collapses are generally preceded by a period of accelerating deformation due to internal fracturing that is enhanced by the presence of fluids (Kilburn and Petley 2003). Hence, in the case of the 2010 Mount Meager failure, there was no singular distinct triggering event, but rather a combination of destabilizing factors, including the long summer heatwave that contributed, over time, to the collapse. The increase in the number and size of faults and the precursory failures at the toe of the slope in the years prior to the landslide suggest that slow acceleration could have been detected using monitoring methods such as photogrammetry, LIDAR, InSAR, in-situ strain meters, or GPS. If so, it might have been possible to predict the approaching failure by extrapolating the linear inverse-deformation rate trend (Kilburn and Petley 2003; Rose and Hungr 2007; Carlà et al. 2017; Loew et al. 2017).

Alpine glaciers around the world are receding due to climate warming (Liggins et al. 2013). In many mountain ranges, most glaciers will disappear by the end of this century (DeBeer and Sharp 2007; Schiefer et al. 2007; Clarke et al. 2015). Glacier retreat will further destabilize steep slopes (Evans and Clague 1994; Huggel et al. 2013) and provide an additional source of water for elevating pore pressures within unstable rock masses, both of which can cause marginally stable slopes to collapse.

Evidence of deep-seated gravitational deformation is widespread on flanks of Mount Meager volcano (Bovis 1990; Read 1990; Jordan 1994; Van der Kooij and Lambert 2002; Roberti et al. 2015). Examples are shown in Fig. 7 and include the eastern flank of Devastation Creek valley (Fig. 7a), the western flank of Plinth Peak (Fig. 7b), and the western flank of Affliction Creek valley (Fig. 7c). Many of these slowly deforming slopes have retreating glaciers at their toes. The 1931 and 1975 Devastation landslides (ca. 3×10^6 m^3, Carter 1932; and ca. 26×10^6 m^3, Mokievsky-Zubok 1977; Fig. 7a) are examples and may represent similar precursors of a larger flank collapse like the 2010 failure. The estimated areas of instability are 3.6×10^6 m^2 at Devastation Creek, 2.7×10^6 m^2 at Plinth Peak, and 1.3×10^6 m^2 at Affliction Creek. Assuming an average depth of failure of 100 m for these gravitational slope instabilities (Kilburn and Petley 2003), volumes of potential future failures are in the range of 3.6×10^8 m^3, 2.7×10^8 m^3, and 1.3×10^8 m^3 for Devastation Creek, Plinth Peak, and Affliction Creek, respectively. Volcanic landslides of this size could travel tens of kilometers downstream and potentially impact settled areas in Pemberton Meadows (Friele and Clague 2004; Simpson et al. 2006). The continuing deformation of these large sagging rock masses can be monitored and used to forecast their possible catastrophic failure. Given that the risk of injury and death downstream has been deemed unacceptable by international standards (Friele et al. 2008), it would seem prudent to implement slope displacement monitoring at Mount Meager.

Conclusion

The south flank of Mount Meager experienced deep-seated gravitational deformation for decades prior to its final catastrophic collapse in August 2010. We have documented pre-event progressive deformation of the slope using historical vertical airphotos to provide insight into the causes of the collapse. In particular, we draw the following conclusions:

1. After substantial retreat in the early twentieth century, Capricorn Glacier advanced between 1948 and 1981 and then rapidly retreated from 1990 to 2006.
2. Major gravitationally generated faults were already present in 1948. They continued to develop, and other cracks formed at the toe of the slope, manifested by sagging and bulging, until the time of the landslide.
3. Lithologies involved in the collapse are, from bottom to top, hydrothermally altered basement rocks and volcanic breccias, block and ash deposits, and rhyodacitic intrusive rocks.
4. The 2010 collapse involved the entire volcanic edifice from the basement to the top of a secondary peak. The collapse started with failure of the basement and basal breccia units. The remaining unsupported block and ash deposits failed next, followed by the intrusive rocks at the peak.
5. The rock mass that failed in 2010 was partially saturated with about 6×10^6 m^3 of water. Immediately after collapse, this water was available to transform the landslide into a highly mobile debris avalanche with multiple rheologies.
6. The volume of 2010 failure is $53 \pm 3.8 \times 10^6$ m^3. This volume is a refinement of a previous estimate and confirms that the event is the largest historic landslide in Canada.
7. Volcanic rocks at Mount Meager had been weakened by hydrothermal alteration and by fracturing caused by deep-seated gravitational deformation. The flank was also weakened by glacial cycles and left unsupported by glacier retreat and toe erosion. The increase in pore water pressures resulting from ice and snow melt during the warm summer of 2010 triggered the landslide.
8. Other very large ($> 100 \times 10^6$ m^3), slowly deforming instabilities are present on Mount Meager volcano. The same destabilizing factors at play in the lead-up to the 2010 landslide are likely to accelerate ongoing deformation and cause more large landslides. Using the event sequence documented here, and with dedicated monitoring, deformation can be tracked and catastrophic failures forecast. Volcanic landslides of this volume can impact populated areas down-valley, resulting in an unacceptable level of risk. We recommend the implementation of slope displacement monitoring at Mount Meager.

Acknowledgments

We thank Rick Guthrie and an anonymous journal reviewer for their helpful comments on a draft of the paper. Discussion with Andreas Kaab and Matt Lato helped us to formulate some of our SfM ideas.

Funding Financial support for the research was provided by NSERC Discovery Grants to Clague and Ward and by the "End of an Arc: The Remarkable Life and Death of a Volcanic Arc" project, a French-Canadian partnership.

References

Allen SK, Gruber S, Ownes IF (2009) Exploring steep permafrost bedrock and its relationship with recent slope failures in the Southern Alps of New Zealand. Permafr Periglac Process 20:345–356

Allstadt K (2013) Extracting source characteristics and dynamics of the August 2010 Mount Meager landslide from broadband seismograms. J Geophys Res Earth Surf 118:1472–1490. https://doi.org/10.1002/jgrf.20110
ASPRS (American Society of Photogrammetry and Remote Sensing) (2014) ASPRS positional accuracy standards for digital geospatial data. Photogramm Eng Remote Sens 81(3) 26 p
Bovis M (1990) Rock-slope deformation at Affliction Creek, southern Coast Mountains, British Columbia. Can J Earth Sci 27:243–254
Bovis M, Jakob M (2000) The July 29, 1998 debris flow and landslide dam at Capricorn Creek, Mount Meager Volcanic Complex, southern Coast Mountains, British Columbia. Can J Earth Sci 37:1321–1334
Capra L (2006) Abrupt climatic changes as triggering mechanisms of massive volcanic collapses. J Volcanol Geotherm Res 155:329–333. https://doi.org/10.1016/j.jvolgeores.2006.04.009
Capra L, Bernal JP, Carrasco-Núñez G, Roverato M (2013) Climatic fluctuations as a significant contributing factor for volcanic collapses. Evidence from Mexico during the Late Pleistocene. Glob Planet Chang 100:194–203. https://doi.org/10.1016/j.gloplacha.2012.10.017
Carlà T, Intrieri E, Di Traglia F, Nolesini T, Gigli G, Casagli N (2017) Guidelines on the use of inverse velocity method as a tool for setting alarm thresholds and forecasting landslides and structure collapses. Landslides 14(2):517–534. https://doi.org/10.1007/s10346-016-0731-5
Carter NM (1932) Exploration in the Lillooet River watershed. Can Alpine J 21:8–18
Cecchi E, van Wyk de Vries B, Lavest JM (2004) Flank spreading and collapse of weak-cored volcanoes. Bull Volcanol 67:72–91. https://doi.org/10.1007/s00445-004-0369-3
Chleborad AF (1997) Temperature, snowmelt, and the onset of spring season landslides in the Central Rocky Mountains. U.S. Geological Survey Open-File Report 97-27, 35 p
Clague JJ, Ward B (2011) Pleistocene glaciation of British Columbia. In Ehlers L, Gibbard PL, Hughes PD (eds.), Quaternary glaciations—extent and chronology: a closer look. Developments in Quaternary Science 15, Elsevier, Amsterdam, Netherlands, p. 563–573. https://doi.org/10.1016/B978-0-444-53447-7.00044-1
Clague JJ, Evans SG, Rampton VN, Woodsworth GJ (1995) Improved age estimates for the White River and Bridge River tephras, western Canada. Can J Earth Sci 32:1172–1179. https://doi.org/10.1139/e95-096
Clarke GKC, Jarosch AH, Anslow FS, Radich V, Menounos B (2015) Projected deglaciation of western Canada in the in the 21st century. Nat Geosci 8:372–377. https://doi.org/10.1038/NGEO2407
D'Agata C, Bocchiola D, Maragno D, Smiraglia C, Diolaiuti GA (2013) Glacier shrinkage driven by climate change during half a century (1954-2007) in the Ortles-Cevedale group (Stelvio National Park, Lombardy, Italian Alps). Theor Appl Climatol 116:169–190. https://doi.org/10.1007/s00704-013-0938-5
DeBeer CM, Sharp MJ (2007) Recent changes in glacier area and volume within the southern Canadian Cordillera. Ann Glaciol 46:215–221
Delcamp A, Roberti G, van Wyk de Vries B (2016) Water in volcanoes: evolution, storage and rapid release during landslides. Bull Volcanol, v 78(12), 12p. doi:https://doi.org/10.1007/s00445-016-1082-8
Detienne M (2016) Volcanic flank and sector collapses: unravelling the role of hydrothermal alteration using combined mineralogical, experimental, and numerical modelling studies. PhD thesis, Université catholique de Louvain, Louvain-la-Neuve, 401 p
Diolaiuti G, Bocchiola D, D'Agata C, Smiraglia C (2012) Evidence of climate change impact upon glaciers' recession within the Italian Alps: the case of Lombardy glaciers. Theoretical and Applied Climatology, v 109, p. 429–445, https://doi.org/10.1007/s00704-012-0589-y
Evans SG, Clague JJ (1994) Recent climatic change and catastrophic geomorphic processes in mountain environments. Geomorphology 10:107–128
FGDC (Federal Geographic Data Committee) (1998) Geospatial positioning accuracy standards. Part 3: National standard for spatial data accuracy. Subcommittee for Base Cartographic Data, U.S. Geological Survey, Reston, VA, 28 p
Finn CA, Sisson TW, Deszcz-Pan M (2001) Aerogeophysical measurements of collapse-prone hydrothermally altered zones at Mount Rainier volcano. Nature 409:600–602
Fonstad MA, Dietrich JT, Courville BC, Carbonneau PE (2013) Topographic structure from motion: a new development in photogrammetric measurements. Earth Surf Process Landf 38:421–430. https://doi.org/10.1002/esp.3366
Friele P (2009) Capricorn Creek debris flow hazard & risk management review. Report to Metro Vancouver Squamish District, Ministry of Forests, Lands and Natural Resource Operations
Friele, P (2012) Volcanic landslide risk management, Lillooet River Valley, BC: Start of North and South FSRs to Meager Confluence, Meager Creek and Upper Lillooet River. Report to Metro Vancouver Squamish District, Ministry of Forests, Lands and Natural Resource Operations
Friele P, Clague JJ (2004) Large Holocene landslides from Pylon Peak, southwestern British Columbia. Can J Earth Sci 41:165–182
Friele P, Jakob M, Clague JJ (2008) Hazard and risk from large landslides from Mount Meager volcano, British Columbia, Canada. Georisk Assess Manag Risk Eng Syst Geohazards 2:48–64. https://doi.org/10.1080/17499510801958711
Gardelle J, Berthier E, Arnaud Y, Kääb A (2013) Region-wide glacier mass balances over the Pamir-Karakoram-Himalaya during 1999–2011. Cryosphere 7:1263–1286. https://doi.org/10.5194/tc-7-1263-2013
Geertsema M, Clague JJ, Schwab JW, Evans SG (2006) An overview of recent large catastrophic landslides in northern British Columbia, Canada. Eng Geol 83:120–143
Glicken H (1996) Rockslide-debris Avalanche of May 18, 1980, Mount St. Helens Volcano, Washington. U.S. Geological Survey Open-File Report 96–677, 90 p., 5 plates, http://pubs.usgs.gov /of /1996 /0677/
Grämiger LM, Moore JR, Gischig VS, Ivy-Ochs S, Loew S (2017) Beyond debuttressing: mechanics of paraglacial rock slope damage during repeat glacial cycles. J Geophys Res Earth Surf 122(4):1004–1036. https://doi.org/10.1002/2016JF003967
Grove JM (1988) The Little Ice Age. Methuen, London 498 p
Gruber S, Haeberli W (2007) Permafrost in steep bedrock slopes and its temperatures-related destabilization following climate change. J Geophys Res Earth Surf 112:1–10. https://doi.org/10.1029/2006JF000547
Gruber S, Hoelzle M, Haeberli W (2004) Permafrost thaw and destabilization of Alpine rock walls in the hot summer of 2003. Geophys Res Lett 31:1–4. https://doi.org/10.1029/2004GL020051
Guthrie RH, Friele P, Allstadt K, Roberts N, Evans SG, Delaney KB, Roche D, Clague JJ, Jakob M (2012) The 6 August 2010 Mount Meager rock slide-debris flow, Coast Mountains, British Columbia: characteristics, dynamics, and implications for hazard and risk assessment. Nat Hazards Earth Syst Sci 12:1–10. https://doi.org/10.5194/nhess-12-1-2012
Harris C, Arenson LU, Christiansen HH, Etzelmüller B, Frauenfelder R, Gruber S, Haeberli W, Hauck C, Hölzle M, Humlum O, Isaksen K, Kääb A, Kern-Lütschg MA, Lehning M (2009) Permafrost and climate in Europe: monitoring and modelling thermal, geomorphological and geotechnical responses. Earth Sci Rev 92:117–171. https://doi.org/10.1016/j.earscirev.2008.12.002
Heap MJ, Wadsworth FB (2016) Closing an open system: pore pressure changes in permeable edifice rock at high strain rates. J Volcanol Geotherm Res 315:40–50. https://doi.org/10.1016/j.jvolgeores.2016.02.011
Heap MJ, Farquharson JI, Baud P, Lavallée Y, Reuschlé T (2015) Fracture and compaction of andesite in a volcanic edifice. Bull Volcanol 77(6), 19 p). https://doi.org/10.1007/s00445-015-0938-7
Hickson CJ, Russell JK, Stasiuk MV (1999) Volcanology of the 2350 BP eruption of Mount Meager Volcanic Complex, British Columbia, Canada: implications for hazards from eruptions in topographically complex terrain. Bull Volcanol 60:489–507
Holm K, Bovis M, Jakob M (2004) The landslide response of alpine basins to post-Little Ice Age glacial thinning and retreat in southwestern British Columbia. Geomorphology 57:201–216
Huggel C (2009) Recent extreme slope failures in glacial environments: effects of thermal perturbation. Quat Sci Rev 28:1119–1130. https://doi.org/10.1016/j.quascirev.2008.06.007
Huggel C, Caplan-Auerbach J, Waythomas CF, Wessels RL (2007) Monitoring and modeling ice-rock avalanches from ice-capped volcanoes: a case study of frequent large avalanches on Iliamna Volcano, Alaska. J Volcanol Geotherm Res 168:114–136. https://doi.org/10.1016/j.jvolgeores.2007.08.009
Huggel C, Caplan-Auerbach J, Wessels R (2008) Recent extreme avalanches: triggered by climate change? Eos 89(47):469–470. https://doi.org/10.1029/2008EO470001
Huggel C, Salzamann N, Allen S (2013) High-mountains slope failures and recent and future warm extreme events. In: McGuire B, Maslin M (eds) Climate forcing of geological hazards. Wiley-Blackwell, Oxford
Huybers P, Langmuir C (2009) Feedback between deglaciation, volcanism, and atmospheric CO_2. Earth Planet Sci Lett 286:479–491. https://doi.org/10.1016/j.epsl.2009.07.014
James MR, Robson S (2012) Straightforward reconstruction of 3D surfaces and topography with a camera: accuracy and geoscience application. J Geophys Res 117:1–17 F03017
Jellinek AM, Manga M, Saar MO (2004) Did melting glaciers cause volcanic eruptions in eastern California? Probing the mechanics of dike formation. J Geophys Res Solid Earth 109:1–10. https://doi.org/10.1029/2004JB002978
Jordan P (1994) Debris flows in the Southern Coast Mountains, British Columbia: dynamic behavior and physical properties. Ph.D. thesis, University of British Columbia, Vancouver, BC
Keiler M, Knight J, Harrison S (2010) Climate change and geomorphological hazards in the eastern European Alps. Philos Transact A Math Phys Eng Sci 368:2461–2479. https://doi.org/10.1098/rsta.2010.0047
Kilburn CRJ, Petley DN (2003) Forecasting giant, catastrophic slope collapse: lessons from Vajont, Northern Italy. Geomorphology 54:21–32. https://doi.org/10.1016/S0169-555X(03)00052-7
Koch J, Menounos B, Clague JJ (2009) Glacier change in Garibaldi Provincial Park, southern Coast Mountains, British Columbia, since the Little Ice Age. Glob Planet Chang 66:161–178. https://doi.org/10.1016/j.gloplacha.2008.11.006
Kolzenburg S, Favalli M, Fornaciai A, Isola I, Harris AJL, Nannipieri L, Giordano D (2016) Rapid updating and improvement of airborne LIDAR DEMs through ground-based SfM

3-D modeling of volcanic features. IEEE Trans Geosci Remote Sens 54:6687–6699. https://doi.org/10.1109/TGRS.2016.2587798
Liggins F, Betts RA, McGuire B (2013) Projected future climate changes in the context of geological and geomorphological hazards. In: McGuire B, Maslin M (eds) Climate forcing of geological hazards. Wiley-Blackwell, Oxford, pp 34–55
Linder W (2009) Digital photogrammetry: a practical course. Springer, Berlin 235 p
Loew S, Gschwind S, Gischig V, Keller-Signer A, Valenti G (2017) Monitoring and early warning of the 2012 Preonzo catastrophic rock slope failure. Landslides 14(2):141–154. https://doi.org/10.1007/s10346-016-0701-y
Matthews JA, Briffa KR (2005) The "Little Ice Age": re-evaluation of an evolving concept. Geografiska Annaler Series A Phys Geogr 87:17–36. https://doi.org/10.1111/j.0435-3676.2005.00242.x
McColl ST, Davies TRH, McSaveney MJ (2010) Glacier retreat and rock-slope stability: debunking debuttressing. 11th Congress of the International Association for Engineering Geology and the Environment, Auckland, Aotearoa, 5–10 September 2010, Auckland, p. 467–474
Micheletti N, Chandler JH, Lane SN (2015) Section 2.2. Structure from Motion (SfM) photogrammetry. In: Cook SJ, Clarke LE, Nield JM (eds.), Geomorphological techniques (online edition). British Society for Geomorphology, London, UK, chapter 2, section 2.2, 12p
Mokievsky-Zubok O (1977) Glacier caused slide near Pylon Peak, British Columbia. Can J Earth Sci 15:1039–1052
Moretti L, Allstadt K, Mangeney A, Capdeville Y, Stutzmann E, Bouchut F (2015) Numerical modeling of the Mount Meager landslide constrained by its force history derived from seismic data. J Geophys Res Solid Earth 120:2579–2599. https://doi.org/10.1002/2014JB011426
NRCan (Natural Resources Canada) (2013) Digital elevation model: product specifications, edition 1.1. Government of Canada, Natural Resources Canada, map information branch, GeoGratis Client Services,11p
Pola A, Crosta G, Fusi N, Barberini V, Norini G (2012) Influence of alteration on physical properties of volcanic rocks. Tectonophysics 566–567:67–86. https://doi.org/10.1016/j.tecto.2012.07.017
Pola A, Crosta GB, Fusi N, Castellanza R (2014) General characterization of the mechanical behaviour of different volcanic rocks with respect to alteration. Eng Geol 169:1–13. https://doi.org/10.1016/j.enggeo.2013.11.011
Rampino MR, Self S, Fairbridge RW (1979) Can rapid climatic change cause volcanic eruptions? Science 206(4420):826–829
Read PB (1978) Geology of Meager Creek Geothermal Area, British Columbia. Geological Survey of Canada Open File 603, map, 1 sheet, scale 1:20000
Read PB (1990) Mount Meager complex, Garibaldi Volcanic Belt, southwestern British Columbia. Geosci Can 17:167–170
Reid ME, Sisson TW, Brien DL (2001) Volcano collapse promoted by hydrothermal alteration and edifice. Geology 29:779–782
Remondino F, Spera MG, Nocerino E, Menna F, Nex F (2014) State of the art in high density image matching. Photogramm Rec 29:144–166
Roberti G, Friele P, van Wyk De Vries B, Ward B, Clague JJ, Perotti L, Giardino M (2017) Rheological evolution of the Mount Meager 2010 debris avalanche, southwestern British Columbia. Geosphere 13(2):1–22. https://doi.org/10.1130/GES01389.1
Roberti G, Ward B, van Wyk De Vries B, Falorni G, Perotti L, Clague JJ (2015) Mount Meager volcano, Canada: a case study for landslides on glaciated volcanoes. Abstract, American Geophysical Union, Fall Meeting, San Francisco, CA
Rose ND, Hungr O (2007) Forecasting potential rock slope failure in open pit mines using the inverse-velocity method. Int J Rock Mech Min Sci 44:308–320
Roverato M, Capra L, Sulpizio R, Norini G (2011) Stratigraphic reconstruction of two debris avalanche deposits at Colima Volcano (Mexico): insights into pre-failure conditions and climate influence. J Volcanol Geotherm Res 207:33–46. https://doi.org/10.1016/j.jvolgeores.2011.07.003
Schiefer E, Menounos B, Wheate R (2007) Recent volume loss of British Columbian glaciers, Canada. Geophys Res Lett, 34, 6 p, L16503, http://doi:https://doi.org/10.1029/2007GL030780
Siebert L (1984) Large volcanic debris avalanches: characteristics of source areas, deposits and associated eruptions. J Volcanol Geotherm Res 22:163–197
Simpson KA, Stasiuk M, Shimamura K, Clague JJ, Friele P (2006) Evidence for catastrophic volcanic debris flows in Pemberton Valley, British Columbia. Can J Earth Sci 43(6):679–689. https://doi.org/10.1139/E06-026
Smith MV, Carrivick JL, Quincey DJ (2015) Structure from motion photogrammetry in physical geography, 40, p. 247–275, doi:https://doi.org/10.1177/0309133315615805
Snavely N, Seitz SN, Szeliski R (2008) Modeling the world from internet photo collections. Int J Comput Vis 80:189–210
Terlien MTJ (1998) The determination of statistical and deterministic hydrological landslide-triggering thresholds. Environ Geol 35(2–3):124–130. https://doi.org/10.1007/s002540050299
Valderrama P, Roche O, Samaniego P, van Wyk de Vries B, Bernard K, Mariño J (2016) Dynamic implications of ridges on a debris avalanche deposit at Tutupaca volcano (southern Peru). Bull Volcanol 78(2), 14p). https://doi.org/10.1007/s00445-016-1011-x
van der Kooij M, Lambert A (2002) Results of processing and analysis of large volumes of repeat-pass InSAR data of Vancouver and Mount Meager (B.C.). Geoscience and Remote Sensing Symposium, IGARSS '02, 2002 I.E. International
van Wyk de Vries B, Francis PW (1997) Catastrophic collapse at stratovolcanoes induced by gradual volcano spreading. Nature 387:387–389
van Wyk de Vries B, Self S, Francis PW, Keszthelyi L (2001) A gravitational spreading origin for the Socompa debris avalanche. J Volcanol Geotherm Res 105:225–247
Voight B, Glicken H, Janda RJ, Douglass PM (1981) Catastrophic rockslide avalanche of May 18. In: Lipman W, Mulineaux DR (eds.), The 1980 eruptions of Mount St. Helens, Washington. US Geological Survey Professional Paper 1250, p. 347–377
Voight B, Komorowski JC, Norton GE, Belousov A, Belousova M, Boudon G, Francis PW, Franz W., Heinrich P, Sparks RSJ, Young SR (2002) The 26 December (boxing day) 1997 sector collapse and debris avalanche at Soufriére Hills volcano, Montserrat. In: Druitt TH, Kokelaar P (eds.), The eruption of Soufriere Hills volcano, Montserrat, from 1995 to 1999.Geological Society of London Memoir 21, p. 363–407
Watt SFL, Pyle DM, Mather TA (2013) The volcanic response to deglaciation: evidence from glaciated arcs and a reassessment of global eruption records. Earth Sci Rev 122:77–102. https://doi.org/10.1016/j.earscirev.2013.03.007
Westoby MJ, Brasington J, Glasser NF, Hambrey MJ, Reynolds JM (2012) Structure-from-motion' photogrammetry: a low-cost, effective tool for geoscience applications. Geomorphology 179:300–314
Wyering LD, Villeneuve MC, Wallis IC, Siratovich PA, Kennedy BM, Gravley DM, Cant JL (2014) Mechanical and physical properties of hydrothermally altered rocks, Taupo Volcanic Zone, New Zealand. J Volcanol Geotherm Res 288:76–93. https://doi.org/10.1016/j.jvolgeores.2014.10.008

Electronic supplementary material The online version of this article (https://doi.org/10.1007/s10346-017-0901-0) contains supplementary material, which is available to authorized users.

G. Roberti (✉) · **B. van Wyk de Vries**
Université Clermont Auvergne, CNRS, IRD, OPGC, Laboratoire Magmas et Volcans,
Campus Universitaire des Cézeaux,
6 Avenue Blaise Pascal, TSA 60026 - CS 60026, 63178, AUBIERE Cedex, France
Email: groberti@sfu.ca

G. Roberti · **B. Ward** · **J. J. Clague**
Earth Sciences Department ,
Simon Fraser University,
8888 University Drive, Burnaby, British Columbia V5A 1S6, Canada

P. Friele
Cordilleran Geoscience,
PO Box 612, Squamish, British Columbia V8B 0A5, Canada

L. Perotti · **M. Giardino**
GeoSitLab - GIS and Geomatics Laboratory Earth Sciences Department,
University of Torino,
Via Valperga Caluso 35, 10125, Torino, Italy